

# Tandem reductive amination and deuteration over a phosphorus-modified iron center

Received: 12 July 2024

Accepted: 20 December 2024

Published online: 21 February 2025

Check for updates

Haifeng Qi<sup>1,2,5</sup>, Yueyue Jiao<sup>1,5</sup>, Jianglin Duan<sup>1,3</sup>, Nicholas F. Dummer<sup>2</sup>, Bin Zhang<sup>2</sup>, Yujing Ren<sup>3</sup>✉, Stuart H. Taylor<sup>2</sup>, Yong Qin<sup>4</sup>, Kathrin Junge<sup>1</sup>✉, Haijun Jiao<sup>1</sup>✉, Graham J. Hutchings<sup>2</sup>✉ & Matthias Beller<sup>1</sup>✉

Deuterated amines are key building blocks for drug synthesis and the identification of metabolites of new pharmaceuticals, which drives the search for general, efficient, and widely applicable methods for the selective synthesis of such compounds. Here, we describe a multifunctional phosphorus-doped carbon-supported Fe catalyst with highly dispersed isolated metal sites that allow for tandem reductive amination-deuteration sequences. The optimal phosphorus-modified Fe-based catalyst shows excellent performance in terms of both reactivity and regioselectivity for a wide range of deuterated anilines, amines, bioactive complexes, and drugs (>50 examples). Experiments on the gram scale and on catalyst recycling show the application potential of this method. Beyond the direct applicability of the developed method, the described approach opens a perspective for the development of multifunctional single-atom catalysts in other value-adding organic syntheses.

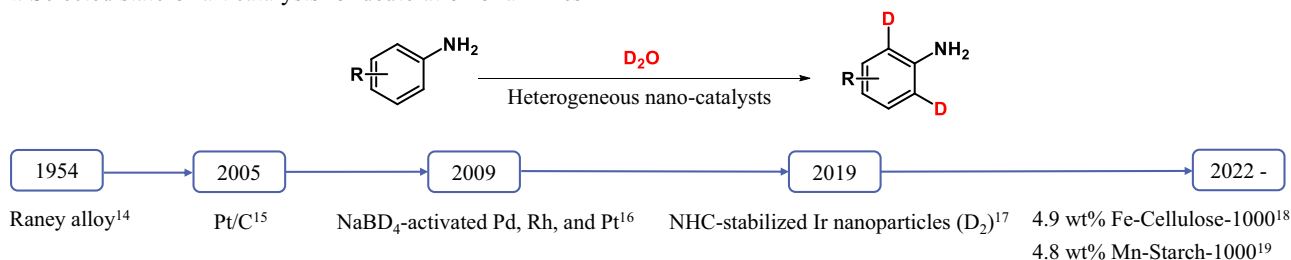
Isotope labeling of amines plays an important role in the development of new pharmaceuticals and agrochemicals, as the introduction of isotopes is used to visualize the progression of bioactive compounds in organisms and nature<sup>1</sup>. One of the most important isotopic labels are deuterium atoms, which are commonly used for mechanistic investigations in organic and organometallic chemistry, too<sup>2</sup>. As a result, numerous synthetic methods for deuterium labeling have been developed, with hydrogen isotope exchange (HIE) proving to be one of the most important methodologies, especially for the late functionalization of bioactive molecules<sup>3–6</sup>. Interestingly, in recent years deuterated organic molecules gained attention as authentic medications themselves due to the potentially extended half-life of the active compound, allowing less frequent dosing, as well as minimizing or avoiding toxic metabolites. The improved pharmacokinetic properties of deuterated analogs of drug molecules are due to the greater stability

of C–D bonds ( $3.0 \pm 1.2$  kJ/mol higher activation energy) against metabolic degradation compared to C–H bonds<sup>7</sup>. Notably, in 2017 the FDA approved the first deuterated drug, Austedo, for the treatment of Huntington’s disease-related disorders<sup>8</sup>. In the same year, Concert Pharmaceuticals sold a deuterated drug, Kalydeco (Ivacaftor), used in treating cystic fibrosis, to Vertex Pharmaceuticals<sup>9</sup>, illustrating the potential for deuterated pharmaceuticals. Since then, many other companies including Teva Pharma, DeuteRx, BMS Pharma, Retrotope, Aclaris Therapeutics, Alkeus Pharma, and Euclises Pharma have expressed their interest in deuterated drugs<sup>9–11</sup>.

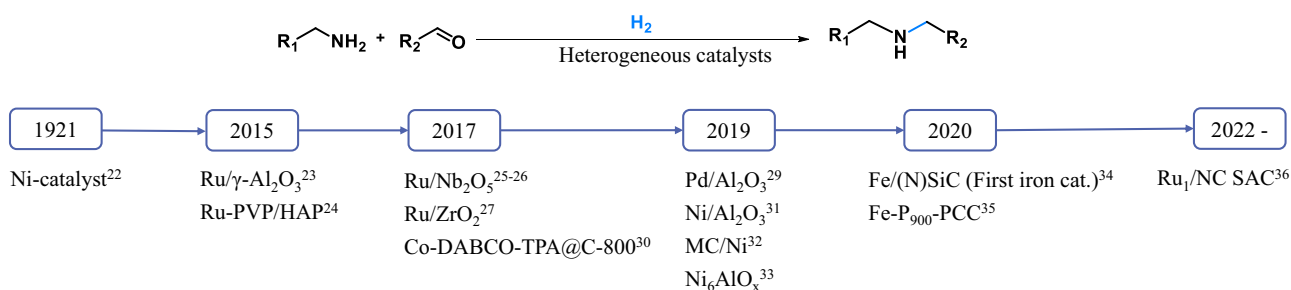
Amino-substituted (hetero)arenes, which account for more than 50% of the 200 best-selling small molecule drugs in 2023<sup>12</sup>, are interesting building blocks for the production of known and new deuterium-labeled drugs. Since the original discovery of Raney alloy catalysts in 1954, many homogeneous and heterogeneous catalysts,

<sup>1</sup>Leibniz-Institut für Katalyse e. V., Rostock, Germany. <sup>2</sup>Max Planck-Cardiff Centre on the Fundamentals of Heterogeneous Catalysis FUNCAT, Translational Research Hub, Cardiff University, Cardiff, UK. <sup>3</sup>Interdisciplinary Research Center of Biology & Catalysis, School of Life Sciences, Northwestern Polytechnical University, Xi’an, China. <sup>4</sup>State Key Laboratory of Coal Conversion, Institute of Coal Chemistry, Chinese Academy of Sciences, Taiyuan, China. <sup>5</sup>These authors contributed equally: Haifeng Qi, Yueyue Jiao. ✉e-mail: [renyj@nwpu.edu.cn](mailto:renyj@nwpu.edu.cn); [kathrin.junge@catalysis.de](mailto:kathrin.junge@catalysis.de); [haijun.jiao@catalysis.de](mailto:haijun.jiao@catalysis.de); [hutch@cardiff.ac.uk](mailto:hutch@cardiff.ac.uk); [matthias.beller@catalysis.de](mailto:matthias.beller@catalysis.de)

## a Selected state-of-art catalysts for deuteration of anilines



## b Selected catalysts for reductive amination



## c Proposed tandem catalytic reductive amination and deuteration over dual-functional Fe single-atom catalyst

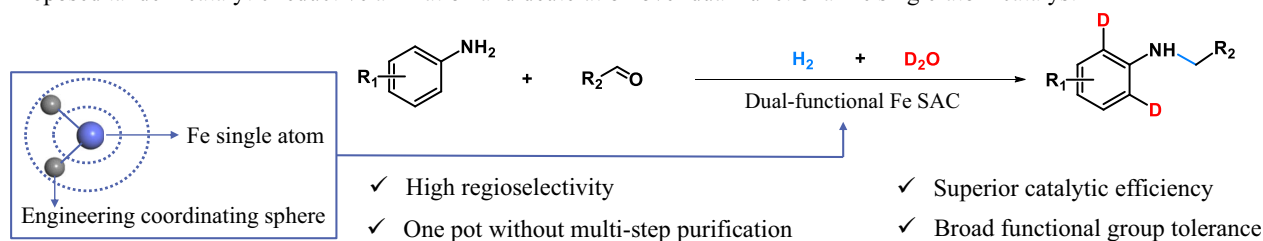


**Fig. 1 | Catalysts development for deuteration and reductive amination reactions.** **a** Selected state-of-the-art catalytic systems for deuterium labeling of anilines, **b** reductive amination catalysts, and **c** this work of tandem catalytic reductive amination and deuteration using dual-functional Fe SAC.

predominantly employing precious metals such as Ir, Pd, Pt, Ru, and Rh, have been reported for the deuterium labeling of anilines (Fig. 1a)<sup>13-17</sup>. In recent years, state-of-the-art Fe- and Mn-based nano-catalysts have also been developed for such transformations<sup>18,19</sup>; however, relatively high metal contents (~20 mol% Fe and ~10 mol% Mn) are required, and the structural heterogeneity of metal nanoparticles makes it difficult to identify active sites for further development of more efficient deuteration catalysts.

To extend the development of deuterated amino-substituted (hetero)arenes, domino and tandem processes are conceptually interesting<sup>20</sup>. Here, further reactions take place under the reaction conditions of the deuteration reaction. Ideally, the catalyst for the corresponding functionalization reaction can be used directly for deuteration. In this context, catalytic reductive amination is an attractive tool for the synthesis of a broad repertoire of amino-substituted compounds<sup>21</sup> and numerous heterogeneous noble nano/cluster catalysts have been developed for such conversions (Fig. 1b)<sup>22-29</sup>. In the past decade, there is a growing interest in alternative non-noble metal catalysts for reductive aminations. More specifically, cobalt, nickel, and the first iron nano-catalysts<sup>30-34</sup>, as well as a few examples of advanced single-atom catalysts (SACs) have been fabricated<sup>35,36</sup>. Based on these principles, the combination of reductive amination and subsequent deuteration reactions has the potential to significantly expand the spectrum of deuterated amine chemicals.

To combine the two desired transformations, namely reductive amination and deuteration of anilines, into a one-pot system, we

envisioned the development of a multifunctional catalyst as essential. Obviously, such a system would improve the reaction efficiency and circumvent the need for tedious synthetic/purification procedures for pre-functionalizations and workup. From both academic and industrial perspectives, constructing a single-atom catalyst with 100% atom utilization efficiency would represent an ideal approach for driving these two reactions<sup>37,38</sup>. Especially Fe-based SAC, owing to the availability, low cost, and biological relevance of iron, among other factors, are interesting<sup>39</sup>. However, unlike sole reductive amination or deuteration processes, conducting such a complex reaction system with single-metal sites poses significant challenges and may be accompanied by poisoning effects from functionalized substrates, intermediates, and/or products<sup>36</sup>. Thus, subtle modifications of the coordinative environment on the metal center are required to construct such a multifunctional single-atom catalyst, a task that remains challenging and relatively underdeveloped.

Herein, we present for the first time a dual-functional phosphorus-doped Fe-SAC that efficiently enables both reductive amination and deuteration using H<sub>2</sub> as a reducing agent and inexpensive D<sub>2</sub>O as a deuterium source (Fig. 1c). We show that the Fe-SAC catalyst developed by us exhibits excellent catalytic performance at remarkably low Fe content (0.2 mol%) and achieves a TOF of 115 h<sup>-1</sup>. It enables the production of various deuterated amines with a broad substrate spectrum and a unique tolerance to functional groups, which also allows late-stage deuteration of natural products and current pharmaceuticals.

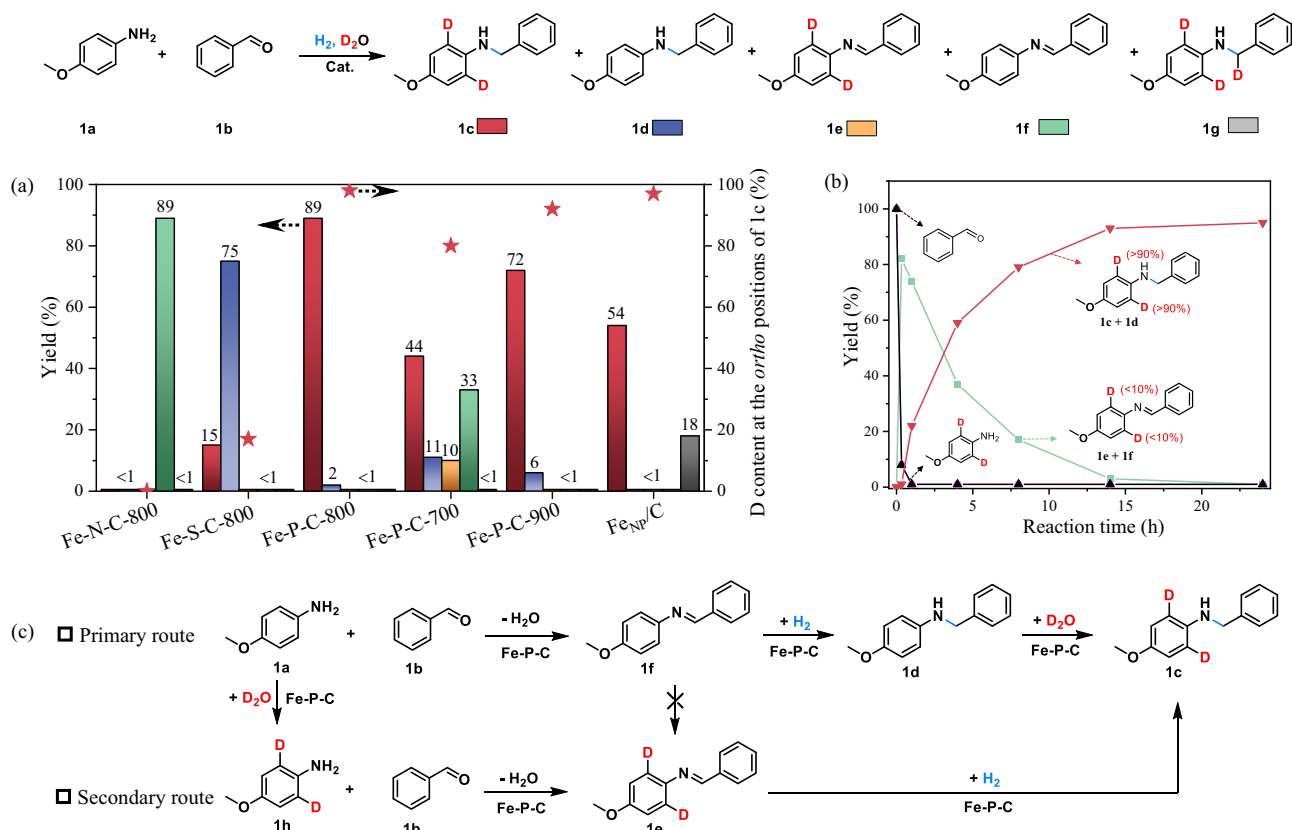


**Fig. 2 | Tandem reductive amination-deuteration of p-anisidine with benzaldehyde<sup>a</sup>.** **a** Catalyst testing, **b** reaction conversion-time profile, and **c** proposed reaction pathway. <sup>a</sup>Reaction conditions: 0.25 mmol **1a**, 0.25 mmol **1b**, 0.2 mol% Fe catalyst (e.g., 20 mg Fe-P-C-800), 90 equiv. D<sub>2</sub>O (405  $\mu$ L), 1 mL

toluene, 40 bar H<sub>2</sub>, 140 °C, 24 h. <sup>b</sup>Fe<sub>NP</sub>/C (Fe-Cellulose-1000) is prepared according to previous work<sup>18</sup>. The NMR of products **1c** + **1d** are shown in Supplementary Figs. 25–26.

## Results and discussion

### Establishing a method of tandem catalytic reductive amination and deuteration

Considering that Fe-based nanocatalysts have previously been proven capable of catalyzing reductive amination and deuteration labeling reactions separately<sup>18,34</sup>, the main challenge here was the development of a dual-functional Fe-based catalyst that can drive both transformations under the same reaction conditions in one pot. Initially, a series of Fe-based materials with different coordination environments were prepared. For example, the P-doped carbon-supported Fe catalyst was prepared by high-temperature pyrolysis of self-assembled precursors, including a mixture of phytic acid, Fe(NO<sub>3</sub>)<sub>3</sub>·9H<sub>2</sub>O, and SiO<sub>2</sub> template, under an argon atmosphere, followed by alkali etching to remove the template<sup>36</sup>.

As the model system, the reaction between readily accessible p-anisidine **1a** and benzaldehyde **1b** was carried out in D<sub>2</sub>O and 40 bar H<sub>2</sub> in the presence of the prepared materials (Fig. 2a and Supplementary Table 1). Notably, these and related substrates find widespread use in the manufacture of pharmaceuticals and pesticides<sup>18</sup>. Inspired by previous work suggesting that Fe-N sites could effectively catalyze the activation of H<sub>2</sub>O for the oxidative C-C cleavage of amine<sup>40</sup>, we started testing N-doped carbon-supported Fe materials. However, the formation of small amounts of amination products indicated the weak hydrogenation ability of Fe-N-C, regardless of their preparation (column 1, Fig. 2a and Supplementary Table 1). This is also evidenced by the fact that Fe-N-C SACs were mainly used in oxidative transformations rather than hydrogenation reactions<sup>41–44</sup>. To realize the desired two reactions with a single catalyst material under the same reaction conditions, we investigated the influence of the coordinative environment of the dispersed metal centers on the catalytic activity

and selectivity<sup>45,46</sup>. Specifically, we synthesized little-known Fe-based materials with S- and P-doped carbon supports and evaluated their performance in the benchmark reaction. Thus, in the presence of S-doped carbon on Fe-S-C materials, a higher amination activity but at the same time a relatively low deuteration content (D) was observed (~17% deuteration content, column 2, Fig. 2a and Supplementary Table 1). Contrary, the Fe catalyst on a P-doped carbon support shows significantly improved activity for the reductive amination reaction with simultaneously high regioselectivity for the *ortho*-deuteration on the aniline ring of **1c** (Fe-P-C, 91% yield with 98% deuteration content, column 3, Fig. 2a). This result is in sharp contrast to our previous findings, where homogeneous catalyst allowed for *ortho*-position deuteration only on the benzaldehyde ring (in the presence of aniline) under similar reaction conditions<sup>47</sup>. In order to further improve the reaction activity and selectivity, the coordination sphere of the active metal centers was further modulated by varying the pyrolysis temperature<sup>36,46</sup>. As a result, the Fe-P-C catalyst, pyrolyzed at 800 °C, exhibited the best performance (columns 3–5, Fig. 2a). In addition, the influence of critical reaction parameters, including temperature, pressure, solvents, and quantity of D<sub>2</sub>O, were investigated and optimized (Supplementary Fig. 1). In conclusion, this tandem catalytic process can be efficiently conducted using 90 equivalents of D<sub>2</sub>O in toluene under 40 bar of H<sub>2</sub> at 140 °C. Interestingly, the Fe<sub>NP</sub>/C (Fe-Cellulose-1000) nano-catalyst described in our previous work<sup>18</sup> showed only moderate reductive amination and deuteration activity but also exhibited specific N-alkyl position deuteration (column 6, Fig. 2a). Apparently, this latter deuteration is a result of the catalytic reduction of the in situ generated imine group (see below). We consider that this deuteration is a result of the different reactivity of Fe nanoparticles<sup>48</sup>, allowing the potential H-D exchange between H<sub>2</sub> and

D<sub>2</sub>O. For comparison, several other heterogeneous catalysts (Cu, Co, and Ni) were prepared and tested in the benchmark reaction, showing moderate reactivity (Supplementary Table 1). Additionally, noble-metal catalysts Ru and Rh, supported on phosphorus-doped carbon, exhibited both reductive amination and deuteration activity (Supplementary Table 1), but with deuteration occurring at the *N*-alkyl position due to their high hydrogenation ability, similar to Fe<sub>NP</sub>/C nano-catalyst. In contrast, commercial Raney Ni and Rh/Al<sub>2</sub>O<sub>3</sub> catalysts only demonstrated reductive amination activity, with negligible deuteration ability (Supplementary Table 1), further highlighting the crucial role of phosphorus incorporation in enhancing deuteration activity.

To demonstrate the intrinsic heterogeneous catalysis of the Fe–P–C SAC, the homogeneous Fe(NO<sub>3</sub>)<sub>3</sub>·9H<sub>2</sub>O and the corresponding organic precursor phytic acid were tested under optimal reaction conditions and both exhibited little activity (Supplementary Table 1). The activity of the heterogeneous material was further verified by a hot-filtration experiment (Supplementary Fig. 2). It is noteworthy that the Fe–P–C catalyst with low Fe loading exhibits two orders of magnitude higher activity (115 h<sup>-1</sup>, Supplementary Table 2) than a Fe nanocatalyst with high Fe loading (5.2 h<sup>-1</sup>), highlighting and emphasizing the effectiveness of this single-atom catalytic system.

In order to clarify the reaction pathway for the formation of the regioselective deuterated product **1c**, several isotope labeling experiments and kinetic profiles in the presence of optimal Fe–P–C catalyst were conducted (Fig. 2b and Supplementary Fig. 3). Initially, deuterated or non-deuterated H<sub>2</sub>O and H<sub>2</sub> were utilized as probe molecules in the reaction (Supplementary Fig. 3). The regioselective deuteration in *ortho*-position of the aniline ring was detected when using D<sub>2</sub>O as the sole deuterated agent, while deuteration at the *N*-alkyl position occurred when D<sub>2</sub> was used as the reaction atmosphere, suggesting the D<sub>2</sub>O contributes to deuteration of the arene ring whereas the H<sub>2</sub> is responsible for hydrogenation in reductive amination. The conversion-time kinetic profiles (Fig. 2b–c) revealed that in the initial stages of the reaction, a significant proportion of the intermediate Schiff base (**1e** or **1f**) with a relatively low D content is produced. The nearly constant D content of Schiff base indicates its hindered deuterated transformation, a notion further supported by a control experiment using **1f** as reaction substrate in the presence of D<sub>2</sub>O (Supplementary Fig. 4). Subsequently, the target deuterated product **1c** accumulates at the expense of the Schiff base. Since Schiff base **1f** (or **1e**) is formed rapidly from the condensation between aniline **1a** and aldehyde **1b**, its slow hydrogenation to the amination product **1d** and the rapid deuteration of **1d** to final **1c** indicate that the hydrogenation of Schiff base should be a rate-determining step, which was further validated by conducting a kinetic isotope effect experiment ( $K_{D_2}/K_{H_2}=1.60$ , Supplementary Table 3). Further kinetic analysis, based on the Arrhenius model of reaction rates, revealed that the hydrogenation of Schiff base **1f** occurs on the surface of the Fe–P–C catalyst, characterized by a small pre-exponential coefficient and a low activation energy (79.0 kJ/mol, Supplementary Fig. 5).

### Structure characterizations and mechanistic investigations

To elucidate the intrinsic structure of the optimal Fe–P–C catalyst, state-of-art characterizations were conducted. Inductively coupled plasma atomic emission spectroscopy (ICP-AES) analysis revealed that the Fe mass loading in the Fe–P–C sample is 0.15 wt% (Supplementary Table 4). The X-ray diffraction (XRD) pattern of the Fe–P–C sample shown merely two broad peaks at 26° and 43° (insert, Fig. 3a), assigned to reflections of the (002) and (101) planes of carbon, respectively, indicating its layered planar structure<sup>49</sup>. The weak and broad (101) peak at 43° suggests that additional P doping leads to a lower degree of graphitic crystallinity and richer defects in the carbon matrix, further confirmed by its broader D and G bands at 1320 cm<sup>-1</sup> and 1596 cm<sup>-1</sup>, respectively, as well as a high-intensity ratio ( $I_D/I_G=1.3$ ) of the D band to the G band in the Raman spectrum (Supplementary Fig. 6)<sup>50</sup>. It is noteworthy that no diffraction peaks corresponding to Fe or FeO<sub>x</sub> are

detected, thus excluding the presence of any large Fe-containing crystalline particles in the Fe–P–C catalyst. Combining these findings with the absence of nanoparticles in low-magnification scanning transmission electron microscopy (STEM) images (Fig. 3a and Supplementary Fig. 7) indicates that any Fe species present are highly dispersed in the carbon matrix. Numerous voids can be observed in STEM images and a high Brunauer–Emmett–Teller (BET) specific surface area of around 514 m<sup>2</sup> g<sup>-1</sup> (Supplementary Fig. 8) reveal a three-dimensional (3D) interconnected and entangled mesoporous architecture. Additionally, energy-dispersive X-ray spectroscopy (EDX) images reveal that Fe, P, and C elements are homogeneously distributed throughout the entire P-doped carbon matrix in the Fe–P–C sample, and the spatially similar distribution of Fe and P signals suggests that P atoms might be adjacent to Fe species (Fig. 3b and Supplementary Fig. 9). Most evidently, sub-Ångström-resolution high-angle annular dark-field scanning transmission electron microscopy (HAADF-STEM) was employed to probe the highly dispersed Fe-containing species. The representative images (Fig. 3c and Supplementary Fig. 10) clearly demonstrate that the Fe species (bright dots) are atomically dispersed on the P-doped carbon materials. The signal intensity ratio of Fe<sub>L</sub> and P<sub>L</sub> atoms is around 2.2, following an atomic number ( $Z$ ) contrast image-forming principle  $Z^{1.7}$ , which suggests that the relative bright and dark spots correspond to the Fe and P atoms, respectively, indicating the possible formation of Fe–P coordination in the Fe–P–C material.

X-ray photoelectron spectroscopy (XPS) and X-ray absorption spectroscopy (XAS) characterizations were further conducted to determine the chemical states and electronic interaction between Fe and P. Compared with pristine P-C (1.9 at.% P), the higher P contents (3.1 at.%) together with negative shifts of the characteristic peaks, as well as the emergence of Fe–P species in the high-resolution P 2*p* XPS spectra suggest that Fe and P may stabilize each other in the carbon matrix by forming Fe–P coordination in Fe–P–C (Fig. 3d and Supplementary Table 5). Figure 3e displays the X-ray absorption near edge structure (XANES) spectrum of P *L*<sub>2,3</sub> edge. Peaks a and b at the low-energy side are due to transitions from spin-orbit split 2*p* electrons (the 2*p*<sub>3/2</sub> and 2*p*<sub>1/2</sub> levels, respectively) into the first unoccupied 3*s*-like antibonding state<sup>51</sup>. It can be observed that both peaks show a significant increase after the introduction of P, indicating electron transfer from P to Fe due to potential Fe–P hybridization. At higher energy, a broad and intense peak owing to 2*p* to 3*d* transitions can be observed at around 147–155 eV, which is sensitive to the molecular symmetry and to the local chemical environment of P, often referred to as the 'shape resonance'<sup>51</sup>. The higher intensity of this broad peak for Fe–P–C compared to P–C also suggests possible Fe–P interaction. Figure 3f displays the XANES at the Fe *K*-edge of the Fe–P–C catalyst and references. The edge energy ( $E_0$ ) for the Fe–P–C sample is lower than that of Fe<sub>2</sub>O<sub>3</sub> yet higher than that of iron phthalocyanine (FePc), suggesting Fe atoms carry positive charges + $\delta$  ( $2 < \delta < 3$ , Fig. 3f and Supplementary Table 6), consistent with the XPS characterization results (Supplementary Fig. 11). The coordination environment of Fe single atoms is determined by the extended X-ray absorption fine structure spectra (EXAFS). In the Fourier-transformed EXAFS spectrum, a dominant peak at -1.63 Å is observed in Fe–P–C, which is slightly longer than the Fe–N peak observed at -1.44 Å in FePc and can be associated with the existence of a Fe–P path due to the relatively longer Fe–P bond length (Fig. 3g)<sup>52,53</sup>. Additionally, the Fe–Fe peak at -2.24 Å that appears in Fe foil is not detected in Fe–P–C, confirming the atomic dispersion of Fe. To further discriminate the coordination atoms in Fe–P–C, 2D EXAFS wavelet transform analysis was conducted, a more powerful technique with high resolution in both *k* and *r* space (Fig. 3h–i and Supplementary Fig. 12)<sup>54</sup>. The only observed lobe appears at (4.1 Å<sup>-1</sup>, 1.6 Å) for Fe–P–C, markedly distinct from that for Fe foil (7.7 Å<sup>-1</sup>, 2.2 Å) and FePc (3.8 Å<sup>-1</sup>, 1.4 Å), indicating that the Fe species exist as mononuclear centers and also validating the assignment of the

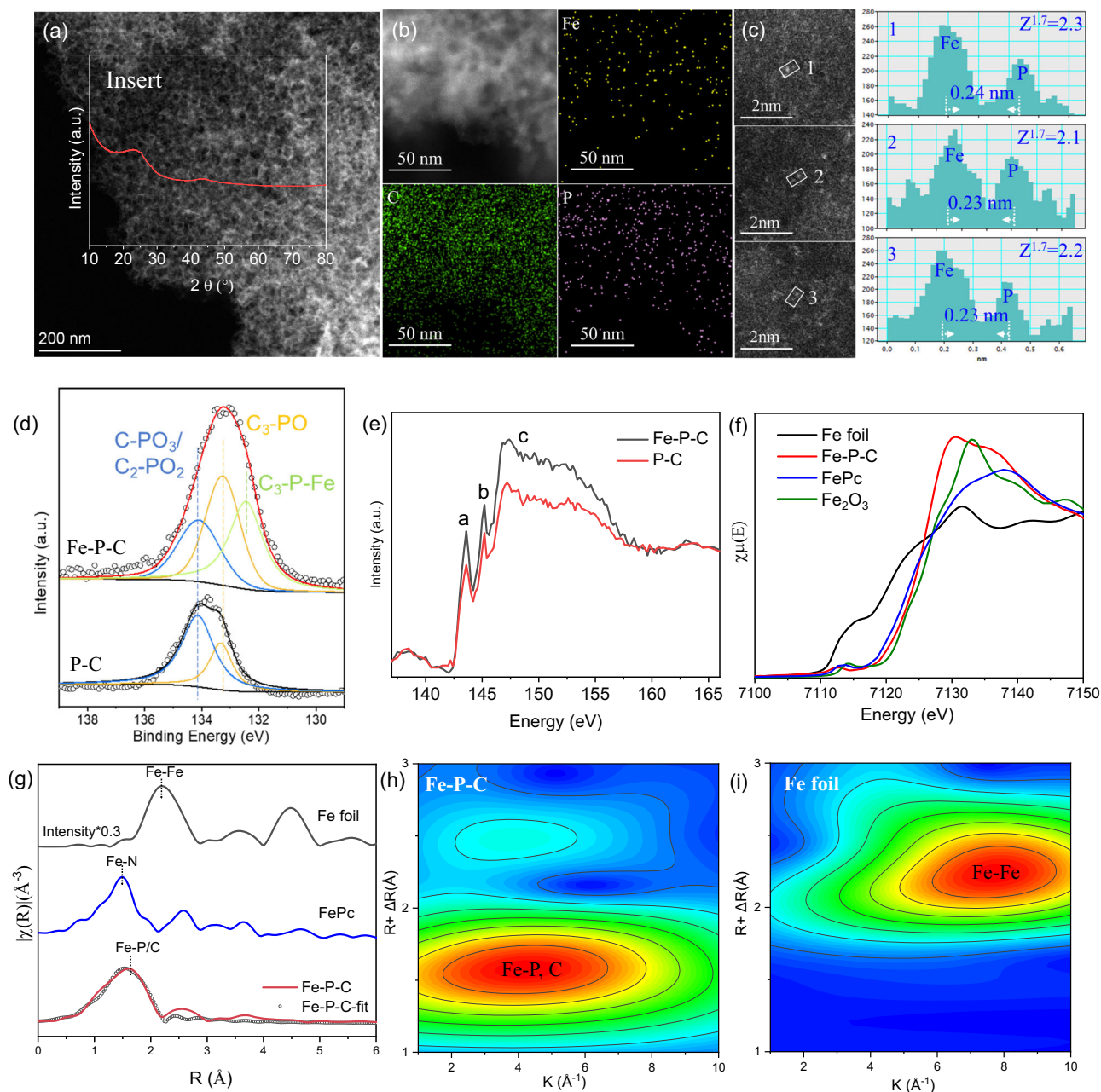


**Fig. 3 | Synthesis and structure characterizations of Fe-P-C SAC.** **a** The scanning transmission electron microscopy image (insertion: X-ray diffraction), **b** elemental mapping of Fe/P/C, **c** high-angle annular dark-field scanning transmission electron microscopy image (the relative bright and dark white dots are Fe atoms and P atoms respectively,  $Z = \text{atomic mass}_{\text{Fe}}/\text{atomic mass}_{\text{P}}$ ), **d**  $2p$  X-ray photoelectron spectroscopy, **e** the normalized X-ray absorption near-edge spectra (XANES) at the

$\text{Fe } L_{2,3}$ -edge, **f** the XANES at the Fe  $K$ -edge (FePc: iron phthalocyanine), **g** the  $k^2$ -weighted Fourier transform extended X-ray absorption fine structure spectra (EXAFS) in  $r$ -space ( $k$  is the wavenumber,  $k = (2m_e(E - E_0))^{1/2}/\hbar$ , where  $\hbar$  is Planck's constant), **h** wavelet transformation for the  $k^2$ -weighted EXAFS signal, and **i** EXAFS fitting curve in the region of 1.0–2.3 Å, shown in  $k^2$ -weighted  $r$ -space of Fe-P-C SAC and references.

scattering contribution from another heavier element (P) as the Fe-P pair in Fe-P-C. Then, the quantitative structural parameters for the first coordination sphere of Fe were extracted by least-squares EXAFS curve-fittings, manifesting the Fe-P and Fe-C coordination numbers (CN) of 1.2 and 3.1, with average absorber-backscattered distances ( $R$ ) of 2.30 Å and 2.00 Å, respectively (Fig. 3g, Supplementary Fig. 13, and Supplementary Table 7). Based on this, we constructed the  $\text{FeP}_1\text{C}_3$  site at a two-carbon-defected site of the graphene monolayer for density functional theory (DFT) calculations. The optimized average bond lengths of Fe-P and Fe-C are 2.13 Å and 1.92 Å, respectively, showing good agreement with experimental values (Supplementary Table 8). The charge density difference and projected density of states (PDOS)

analyses of Fe-P-C identify strong orbital interaction for the Fe-P bonding, as evidenced by significant charge accumulation between Fe and P atoms, as well as substantial overlap between the energy levels of Fe  $3d_{xz}$  and P  $3p_z$  orbitals (Supplementary Fig. 14), which are also corroborated by data illustrated in Fig. 3c–g, and consequently, both Fe and P centers are positively charged, and the neighboring C center are negatively charged, in line with their difference in electronegativity (1.80/Fe, 2.235/P, and 2.544/C)<sup>55</sup>.

On the basis of the above results, the catalytic behavior of  $\text{FeP}_1\text{C}_3$  in reductive amination and deuteration was explored using the DFT method, with computational details outlined in the Methods section. The reaction-time profile (Fig. 2b) shows that the first step involves the

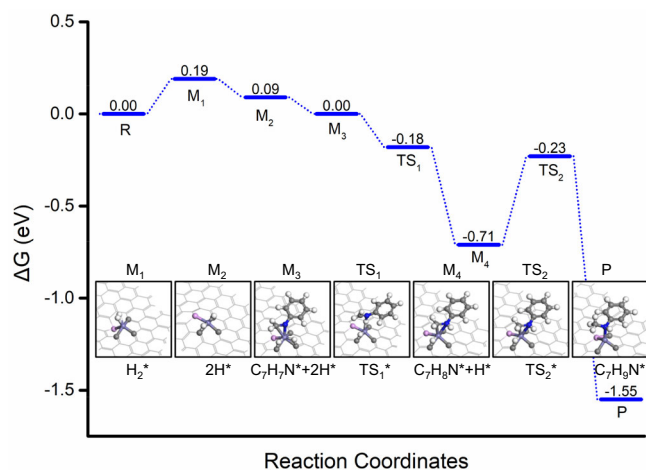


**Fig. 4 | DFT calculation.** The relative Gibbs free energy ( $\Delta G$ ) profiles of imine hydrogenation on  $\text{FeP}_1\text{C}_3$  (colors represent: purple: iron, pink: phosphorus, gray: carbon, blue: nitrogen, white: hydrogen).

rapid dehydration and condensation of aniline with benzaldehyde to form a Schiff base intermediate, followed by its slower hydrogenation to produce a secondary aniline. The final deuteration of secondary aniline is faster, indicating the hydrogenation of the Schiff base is the rate-determining step in this tandem reaction. Thus, our primary focus was on calculating the imine hydrogenation step. As illustrated in Fig. 4 and Supplementary Fig. 15, initial calculations were conducted with the hydrogenation of a simplified benzyl imine intermediate ( $\text{Ph}-\text{CH}=\text{NH}$ ).

Under the reaction condition (140 °C and 40 bar), the dissociative  $\text{H}_2$  adsorption with one H atom on Fe and one H atom on Fe–C bond ( $\text{M}_2$ ) is slightly endergonic by 0.09 eV, indicating the need of high  $\text{H}_2$  pressure for the reaction (Supplementary Figs. 16–17). Then, the co-adsorption of benzyl imine ( $\text{C}_7\text{H}_7\text{N}^*$ ,  $\text{M}_3$ ) leads to the transfer of the H atom on the Fe center and also to the Fe–C bond, with the conjugated C=N bond attaching to the Fe atom, which results in an exergonic process by 0.19 eV. Bader Charge analyses (Supplementary Fig. 18) of  $\text{M}_3$  reveal that the negatively charged N atom (−1.14 e) of the C=N bond is more likely to react with the positively charged H atom (0.06 e) on Fe–C, compared with the positively charged C atom (0.32 e) of the C=N bond. As a result, the hydrogenation of the N atom proceeds with no barrier ( $\text{TS}_1$ ) and is exergonic by 0.71 eV ( $\text{M}_4$ ). Finally, the formation of *N*-methylaniline ( $\text{C}_7\text{H}_6\text{N}^*$ ) requires a free energy barrier of 0.48 eV ( $\text{TS}_2$ ) and is exergonic by 0.84 eV (P). Throughout the entire process, the rate-determining step is the activation of  $\text{H}_2$ , as further supported by the pressure-dependent yields, which show reduced yields at pressures below 40 bar  $\text{H}_2$  (Supplementary Fig. 1b). A slight discrepancy in the energy barriers between experiment and theory (Supplementary Fig. 5 and Supplementary Fig. 17) was observed for imine hydrogenation, likely due to the simplified nature of theoretical models and the complexities of experimental conditions. Corresponding energy profiles and discussion are also provided in Supplementary Fig. 19.

Following the hydrogenation steps, the tandem deuteration reaction is initiated. The activation of  $\text{H}_2\text{O}^*$  occurs on Fe–P/C sites and can have two configurations (Supplementary Fig. 20), in which  $\text{OH}^*$  is favorable on the Fe atom and  $\text{H}^*$  on the P or C atoms (−0.26 eV vs −0.29 eV), potentially resulting in the formation of protonated intermediates (Supplementary Fig. 21). Notably, regioselective *ortho*-position protonated intermediates on the aniline ring are most stable and highly favored, while the *meta*-position protonated intermediates are less stable by around 0.5 eV. On the contrary, the *ortho*-, *meta*- and *para*-position protonated intermediates of the benzylic ring are much higher in energy by 0.9–1.2 eV. This provides a reliable explanation of

the solely regioselective *ortho*-position deuteration observed on the aniline ring.

To further validate this proposed reaction mechanism, several specific poisoning experiments were conducted with the reductive amination and deuteration reactions, separately (Supplementary Fig. 22). Both reactions exhibited a significant decrease in activity when the Fe single-atom sites were poisoned by  $\text{SCN}^-$ , underscoring the pivotal role of Fe species in the hydrogenation and deuteration processes<sup>42</sup>. As anticipated, when the P sites were quenched by  $\text{S}^{3-}$ , the activity of deuteration markedly decreased, while the performance of reductive amination only exhibited modest degradation, which suggests that the P sites primarily contribute to  $\text{D}_2\text{O}$  activation. These experimental results are consistent with the predictions from the DFT calculations.

### One-pot synthesis of diverse deuterated anilines via tandem catalysis

With the optimized Fe–P–C catalyst in hand, we investigated its functional group tolerance by applying diverse substrates. As depicted in Fig. 5a, for aromatic aldehydes with electron-donating/withdrawing groups (**2c–7c**) and aliphatic aldehydes (**8c–10c**), high yields (55–93%) and deuteration content (>80%) of the produced anilines are achieved. Functional groups including methoxy, halides, and trifluoromethyl, as well as more challenging ones, e.g., boronate ester, heterocycles, and unsaturated alkene groups are well tolerated. The latter case (**9c**) is particularly interesting, as conventional noble metal catalysts used in reductive aminations hydrogenate such functional groups. Compared to aromatic aldehydes, the reductive amination of aliphatic aldehydes can be hindered by the unproductive aldol condensation that occurs under basic conditions. Nevertheless, several aliphatic substrates yield the corresponding anilines in very good yields (up to 94%) and high deuterium content ( $\geq 93\%$ , **8c–9c**) in the presence of the Fe–P–C catalyst. Particularly noteworthy is the effective conversion of the biomass-derived building block furfural (**10c**), which is inexpensive (1.0–1.2 €  $\text{kg}^{-1}$ ) and readily available on large scale from biomass (>200 kT per year)<sup>28</sup>. Such state-of-the-art conversion to produce deuterated amines has rarely been reported compared to earlier routes of furfural amination (Supplementary Fig. 23)<sup>56</sup>. In general, the respective amines are labeled at the *ortho*- or *para*-position to the amine group, which can be explained for electronic reasons. However, a simple trick makes it easy to achieve deuteration in the *meta*-position on the aniline ring. More precisely, fully deuterated aniline is used as a substrate and the reaction is carried out in water ( $\text{H}_2\text{O}$ ). In such a case, D–H exchange reactions take place in *ortho*- and *para*-position, with the deuterium atoms remaining in *meta*-position. In addition,  $^2\text{D}$ - and simultaneously  $^{13}\text{C}$ -labeled products can be obtained with specific substrates (**11–12c**). It is worth noting that reductive amination and deuteration of more challenging substrates such as diamines and ketones also proceed well to yield the corresponding deuterated anilines (**13–16c**).

As described in the introduction, amino-substituted (hetero)arenes serve as versatile building blocks for the synthesis of several different products used in agrochemicals and pharmaceuticals<sup>12</sup>, therefore the reactivity of various functionalized anilines was further investigated (Fig. 5b). Encouragingly, the Fe–P–C catalyst enables the effective reductive amination and deuteration of 17 different anilines with excellent chemo- and regioselectivity (**17–33c**). Various halogen-containing (chlorine and fluorine) anilines afforded the deuterated products (**18–21c**, **26c**) without significant dehalogenation side reactions, a common problem observed when using noble metal-based catalysts. Even difficult heterocyclic anilines such as 1-phenylpiperazine, which could not be deuterated in our previous work<sup>18</sup>, underwent reductive amination and deuteration of this molecule efficiently with this catalyst system (**29c**). Additionally, sulfur-containing substrates known to poison noble metal catalysts, exhibited good performance under standard reaction conditions (**23c** and **30c**). We

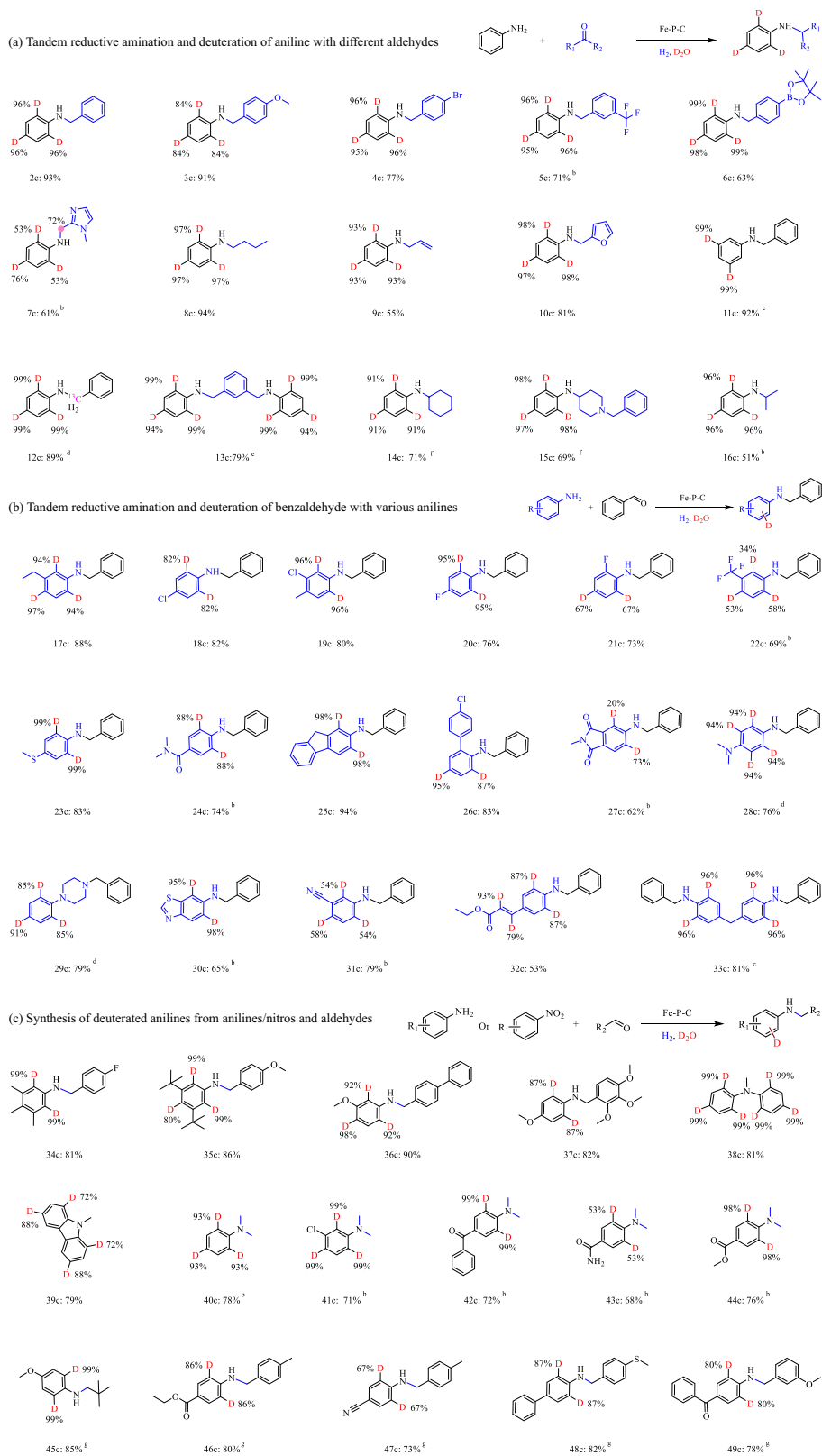


**Fig. 5 | Substrate scope.** **a–c** Tandem reductive amination and deuteration of different amino-substituted (hetero)arenes and aldehydes. <sup>a</sup>Reaction conditions: 0.25 mmol amino-substituted (hetero)arenes, 0.25 mmol aldehydes, 0.2 mol% Fe catalyst (20 mg Fe–P–C-800), 90 equiv. D<sub>2</sub>O (405 μL), 1 mL toluene, 40 bar H<sub>2</sub>, 140 °C, 24 h; <sup>b</sup>150 °C; <sup>c</sup>*N*-benzyl-2,3,4,5,6-pentadeuterioaniline as substrate, H<sub>2</sub>O as

additive; <sup>d</sup>benzaldehyde- $\alpha$ -<sup>13</sup>C as substrate; <sup>e</sup>0.5 mmol benzaldehyde; <sup>f</sup>160 °C; <sup>g</sup>corresponding nitro compound as substrate. Subscripts under product represents isolated yields; the numbers around D represent the deuterium incorporation; the NMR spectra of products can be found in Supplementary Figs. 27–121.

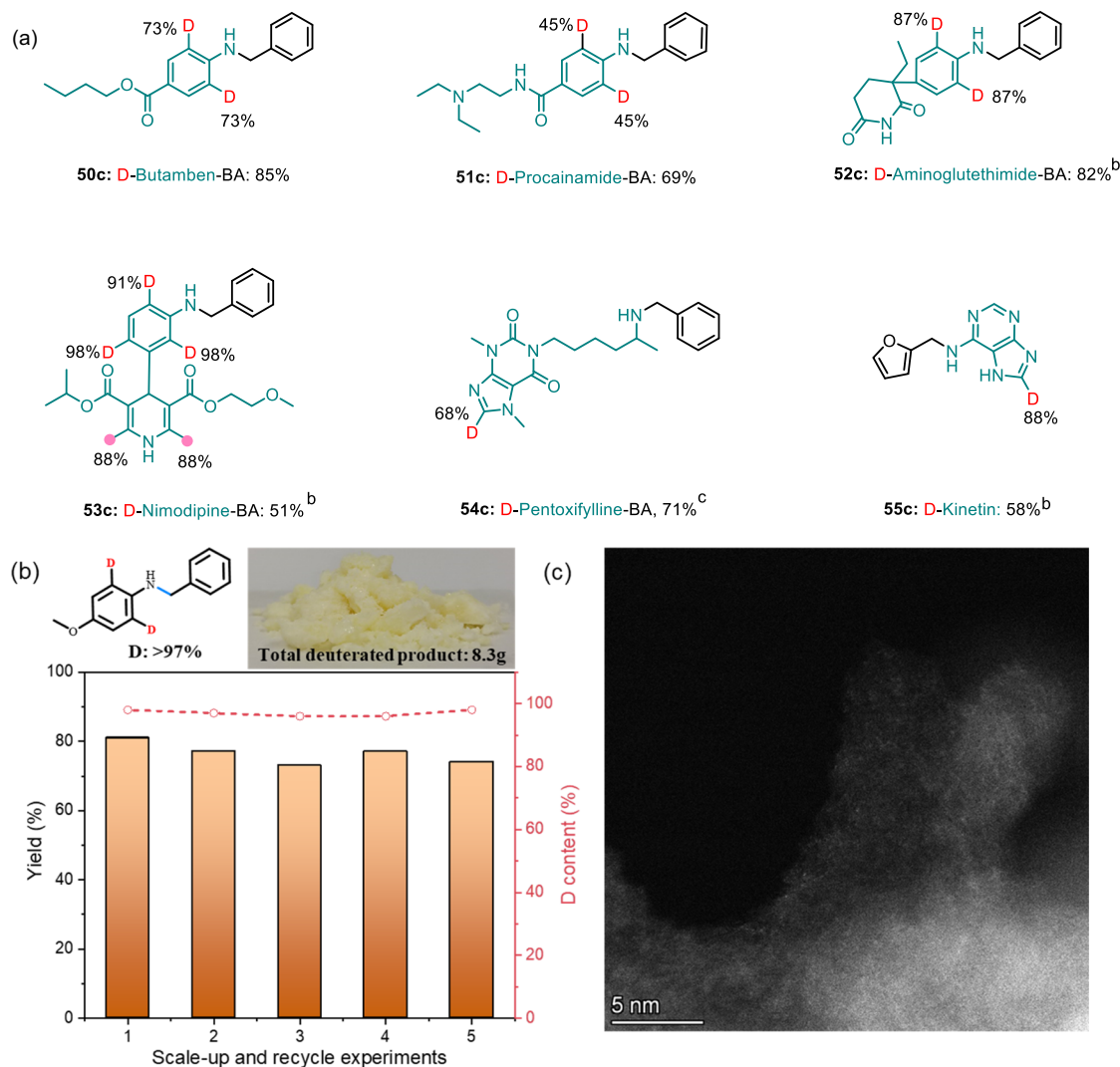


**Fig. 6 | Applications.** **a** Selected synthesis of deuterated bio-active and drug molecules: showcasing the applicability of this domino transformation<sup>a</sup>, **b** scale-up recycling experiments,<sup>d</sup> and **c** HRTEM of used Fe-P-C catalyst after five recycles. <sup>a</sup>Reaction conditions: 0.25 mmol anilines/amines, 0.25 mmol aldehydes, 0.2 mol% Fe catalyst (20 mg Fe-P-C-800), 90 equiv. D<sub>2</sub>O (405  $\mu$ L), 1 mL toluene, 40 bar H<sub>2</sub>, 140  $^{\circ}$ C, 24 h; <sup>b</sup>150  $^{\circ}$ C; <sup>c</sup>reductive amination in toluene for 12 h, then adding D<sub>2</sub>O for

continuing 12 h reaction; <sup>d</sup>10 mmol *p*-anisidine **1a**, 10 mmol **1b**, 1.0 g Fe-P-C-800 catalyst, 40 mL D<sub>2</sub>O, 150 mL toluene, 60 bar H<sub>2</sub>, 150  $^{\circ}$ C, 24 h. Subscripts under products represent isolated yields; the numbers around D represent the deuterium incorporation; the NMR spectra of products can be found in Supplementary Figs. 121–132.

further explored the synthesis of deuterated multi-substituted anilines, commonly found in biologically active and natural products (Fig. 5c, **34c–37c**). *N*-Methylamines are of particular interest due to their role in regulating biological functions, typically prepared through Pd/C-catalyzed reductive amination with formaldehyde. Using our Fe-P-C catalytic system, we synthesized regioselective deuterated *N*-methylanilines starting from formaldehyde and the corresponding anilines (**38–44c**). The Fe-catalyzed synthesis of *N*-methylamines presented here is either more cost-effective or waste-free compared to traditional alkylation methods. Furthermore, the presented reductive amination and deuteration can be extended to nitroarenes as starting materials. Accordingly, deuterated anilines (**45–49c**) were selectively prepared via a domino-hydrogenation-deuteration-condensation-hydrogenation approach. Considering the four chemical transformations involved, the observed yields (73–85%) are excellent.

#### Synthesis of deuterated pharmaceuticals and scale-up recycling applications

To demonstrate the applicability of this heterogeneous Fe-P-C catalytic system towards more functionalized and sensitive organic

molecules which are typically used in life sciences, the deuteration of six natural products and drugs was studied. As depicted in Fig. 6a, the reductive amination-deuteration transformation of Butamben **50c**, Procainamide **51c**, Aminoglutethimide **52c**, Nimodipine **53c**, and Pentoxifylline **54c** proceeded smoothly (51–85% yield) and good to excellent D content (45–98%). Apparently, the presented methodology provides a useful synthetic tool for obtaining deuterated drugs. Of particular interest to us was the deuterated modification of Kinetin, commonly used in cosmetic products as an anti-aging agent, which can be directly obtained from bio-based furfural (**55c**, Supplementary Fig. 23). This novel transformation expands the range of amination products of furfural and paves a new way for the utilization of such abundant bio-platform molecules.

In addition to potential cost advantages of such iron-based materials, recyclability and scalability are crucial features for any applications of heterogeneous catalysts, which can also considerably facilitate product purification. As shown in Fig. 6b, our Fe-P-C SAC exhibits moderate stability and can be conveniently recycled up to five times at gram scale. The slight decrease in activity could possibly be attributed to the loss of the catalyst materials during the recycling

process. Following purification, bright yellow deuterated products were obtained in 10 g-scale. Furthermore, transmission electron microscopy images indicated used Fe–P–C SAC did not show aggregation of the Fe species after recycling (Fig. 6c and Supplementary Fig. 24, compared with Fig. 3a–c).

In summary, we have successfully synthesized a heterogeneous iron-based catalyst with two functions by specifically modifying the coordination environment of atomically distributed Fe centers. The optimal material uses a phosphorus-doped carbon support which, in combination with the Fe centers, enables the activation of H<sub>2</sub> and D<sub>2</sub>O. This makes it possible to carry out catalytic one-pot tandem processes for reductive amination and deuteration reactions to produce directly deuterated anilines/amines. Kinetic profiling and control experiments helped elucidating the tandem catalytic process, wherein reductive amination precedes deuteration due to the hindered deuteration of imine intermediates. Coupled with DFT calculation and key control experiments, we have shown that the Fe–P/C pair sites exhibit moderate activation ability for D<sub>2</sub>O, while the Fe sites facilitate H<sub>2</sub> activation, which working together enable the tandem catalysis to be effectively achieved. We hope our findings provide guidance and inspiration into the construction of atomically dispersed catalysts for achieving multi-component organic transformations, offering understanding critical for catalyst design.

## Methods

### Materials

Phytic acid solution (50 wt% in H<sub>2</sub>O) was purchased from TCI. AERO-SIL<sup>®</sup> fumed silica were purchased from Evonik. Fe (NO<sub>3</sub>)<sub>3</sub>·9H<sub>2</sub>O, *p*-anisidine and benzaldehyde were obtained from Sigma-Aldrich. D<sub>2</sub>O was purchased from Eurisotop. The benzaldehyde was purified by bulb-to-bulb distillation under reduced pressure. All the other chemical reagents were used as received without further purification.

### Catalyst preparation

All catalysts were prepared by a template-sacrificial approach. As an example, for the preparation of Fe–P–C-800 catalyst, a mixture of 30 mg Fe (NO<sub>3</sub>)<sub>3</sub>·9H<sub>2</sub>O and 4 g phytic acid solution (50 wt% in water) was added to 50 mL H<sub>2</sub>O and stirred under reflux at 120 °C for 30 min, followed by addition of 2.0 g fumed silica and stirred at 120 °C for 12 h. Then, the reflux condenser was removed to slow evaporation of H<sub>2</sub>O for 24 h. After the evaporation of solvent and ensuring complete drying, the remaining solid was transferred to a crucible in the furnace and fluxed with argon. The oven was then heated to 800 °C in Argon atmosphere at a ramp rate of 5 °C/min and was held at 800 °C for 2 h. The obtained black powder was washed twice by 50 mL 1 mol/L NaOH solution at 90 °C for 12 h to remove the SiO<sub>2</sub> support. The recovered solid was washed with 2 L water until the filtrate became neutral and then dried at 80 °C for 12 h. The resultant sample was labeled as Fe–P–C-800. Unless otherwise stated in manuscript, Fe–P–C also represents Fe–P–C-800. The samples pyrolyzed at 700 °C and 900 °C were labeled as Fe–P–C-700 and Fe–P–C-900, respectively. In the same procedure, Fe–N–C and Fe–S–C materials were synthesized applying the corresponding N/S-containing organic precursors 1,10-phenanthroline and 2,2-bithiophene, respectively. The P–C sample was synthesized using P-containing organic precursors triphenylphosphine without Fe salts.

### Reaction tests

In the typical reaction, 0.25 mmol *p*-anisidine 1a, 0.25 mmol benzaldehyde 2a, 20 mg Fe–P–C catalyst, 405 μL D<sub>2</sub>O, 1.0 mL toluene were put into an 8 mL vial fitted with magnetic stirring bar and septum cap. A needle was inserted in the septum which allows gaseous reagents to enter. The vials (up to seven) were set in an alloy plate and then placed into a 300 mL steel Parr autoclave. After sealing the autoclave, the autoclave was purged with N<sub>2</sub> for three times and H<sub>2</sub> for three times

and charged with 40 bar H<sub>2</sub> at room temperature. Then the reaction mixture was stirred at a rate of 500 r/min and heated at 140 °C for 24 h. After the reaction, the crude media was extracted with EtOAc (3 × 4 mL), then the organic phase was intensively shaken in presence of 4 mL of H<sub>2</sub>O (e.g., ND<sub>2</sub> → NH<sub>2</sub>) and this aqueous phase was further extracted with EtOAc (3 × 4 mL). The combined organic phases were dried by anhydrous Na<sub>2</sub>SO<sub>4</sub>. Then the isolated product was obtained by column purification using pentane/EtOAc mixture as flow phase and submitted to NMR analysis for determination of the deuterium content.

The yield of 1c or 1d (Y<sub>1c</sub> or Y<sub>1d</sub>) and the deuterium content of 1c + 1d (D<sub>1c+1d</sub>) were calculated using the following equations:

$$Y_{1c+1d}(\%) = (\text{mol}_{1c+1d\text{isolated}}) / (\text{mol}_{1a\text{fed}}) * 100 \quad (1)$$

$$D_{1c+1d}(\%) = \left( 1 - \frac{\text{Corresponding}^1\text{HNMR peak area}_{1c+1d\text{produced}}}{\text{Corresponding}^1\text{HNMR peak area}_{1c\text{standard}}} \right) * 100 \quad (2)$$

$$Y_{1c}(\%) = Y_{1c+1d}(\%) * D_{1c+1d}(\%) \text{ and } Y_{1d}(\%) = Y_{1c+1d}(\%) * (1 - D_{1c+1d}(\%)) \quad (3)$$

### Reusability test

After each reaction, the catalyst was separated from the reaction system by centrifugation. Then the collected catalyst was successively washed by ethanol (50 mL × 3), and then dried at 80 °C for 2 h. The obtained powder was submitted to the next batch of reaction using the previously described reaction test procedure.

The actual Fe loadings were determined by inductively coupled plasma spectroscopy (ICP-OES) on an IRIS Intrepid II XSP instrument (Thermo Electron Corporation).

### X-ray diffraction (XRD)

Analysis was carried out on a PANalytical X'pert diffractometer using Cu Kα radiation source (λ = 0.15432 nm) with a scanning angle (2θ) of 10°–80°, operated at 40 kV and 40 mA.

### Scanning transmission electron microscopy (STEM) and energy dispersive X-ray spectroscopy (EDS)

Experiments were performed on a JEOL JEM-2100F microscope operated at 200 kV, equipped with an Oxford Instruments ISIS/INCA energy-dispersive X-ray spectroscopy (EDS) system with an Oxford Pentafet Ultrathin Window (UTW) Detector.

The aberration-corrected high-angle annual dark-field scanning transmission electron microscopy (AC-HAADF-STEM) analysis was performed on a JEOL JEM-ARM200F equipped with a CEOS probe corrector, with a guaranteed resolution of 0.08 nm. Before microscopy examination, the sample was ultrasonically dispersed in ethanol for 15–20 min, and then a drop of the suspension was deposited on a copper TEM grid coated with a thin holey carbon film.

### X-ray photoelectron spectroscopy (XPS)

Spectra were obtained on a Thermo ESCALAB 250 X-ray photoelectron spectrometer equipped with Al Kα excitation source and with C as internal standard (C 1s = 284.0 eV).

### Soft X-ray absorption spectroscopy (soft-XAS) spectra

Soft X-ray absorption spectroscopy (soft-XAS) spectra of P L<sub>2,3</sub>-edge were performed at the beamline MCD-A at the National Synchrotron Radiation Laboratory (NSRL) in Hefei, China.

### X-ray absorption spectra (XAS)

X-ray absorption spectra (XAS) including X-ray absorption near edge structure (XANES) and extended X-ray absorption fine structure

(EXAFS) at Fe K-edge of the samples were measured at the beamline 14W of the Shanghai synchrotron radiation facility (SSRF) in China. The output beam was selected by a Si(111) monochromator, and the energy was calibrated against a Fe foil. The data were collected at room temperature under transmission mode.

### Nuclear magnetic resonance spectroscopy (NMR)

Nuclear Magnetic Resonance spectroscopy (NMR) spectra were recorded at room temperature in CDCl<sub>3</sub> or d<sup>6</sup>-DMSO on a 300/400 MHz Bruker DRX-300/400 NMR spectrometer.

### Density functional theory (DFT) calculations

Spin-polarized density functional theory (DFT) computations were performed by Vienna ab-initio simulation package (VASP)<sup>57</sup>. The projector augmented wave pseudo-potentials (PAW)<sup>58</sup> were used to describe the interaction between atomic cores and valence electrons. The Perdew–Burke–Ernzerhof (PBE)<sup>59</sup> functional within the generalized gradient approximation (GGA) were used to get the electron exchange and correlation energies. The cutoff energy was set by 500 eV. The FeP<sub>1</sub>C<sub>3</sub> site was constructed in a 6 × 6 periodic graphene supercell according to the experimental coordination number. The vacuum layers were set by 20 Å. A 1 × 1 × 1 Gamma centered Monkhorst Pack k-point sampling was chosen<sup>60</sup>. Geometry optimizations were pursued until the force on each atom falls below the convergence criterion of 0.02 eV/Å and energies were converged within 10<sup>-5</sup> eV. The climbing–image nudged elastic band (CI–NEB) method<sup>61</sup> combined with the DIMER method<sup>62</sup> was used to search the transition states. The transition state structure is confirmed by only one imaginary frequency in frequencies analysis. All reported energetic data include zero-point-energy (ZPE) correction. The adsorption energy ( $E_{\text{ads}}$ ) of adsorbate ( $X^*$ ) is according to the equation of  $E_{\text{ads}} = E_{X^*/\text{slab}} - E_{\text{slab}} - E_X$ , where  $E_{X^*/\text{slab}}$ ,  $E_{\text{slab}}$ , and  $E_X$  is the optimized total energy of the slab with  $X^*$ , the clean slab, and the free adsorbate ( $X$ ) in gas phase (in a 20 Å × 20 Å × 20 Å cell). The barrier ( $E_a$ ) and the reaction energy ( $E_r$ ) are calculated according to  $E_a = E_{\text{TS}} - E_{\text{IS}}$  and  $E_r = E_{\text{FS}} - E_{\text{IS}}$ , where  $E_{\text{IS}}$ ,  $E_{\text{TS}}$  and  $E_{\text{FS}}$  are the total energies of the corresponding initial state (IS), transition state (TS) and final state (FS), respectively. And the Gibbs free energies of periodic model system are estimated by VASPKIT code<sup>63</sup>.  $G_a$  and  $G_r$  represent Gibbs free energy barriers and Gibbs reaction free energies, respectively, which are calculated by  $G_a = G_{\text{TS}} - G_{\text{IS}}$  and  $G_r = G_{\text{FS}} - G_{\text{IS}}$ .

In addition, the protonation Gibbs free energy at 298 K was computed at the B3PW91<sup>64</sup> level of theory in conjugation with the TZVP<sup>65</sup> all electron basis set and carried out by using the Gaussian 16 program<sup>66</sup>.

### Data availability

Other data are available from the corresponding author upon request. All original data needed to evaluate the conclusions in the paper have already been present in the manuscript and the Supplementary Information (including Supplementary Figs. 1–133 and Tables 1–8).

### References

- Babin, V., Taran, F. & Audisio, D. Late-stage carbon-14 labeling and isotope exchange: emerging opportunities and future challenges. *JACS Au* **2**, 1234–1251 (2022).
- Kopf, S. et al. Recent developments for the deuterium and tritium labeling of organic molecules. *Chem. Rev.* **122**, 6634–6718 (2022).
- Zhang, L. & Ritter, T. A perspective on late-stage aromatic C–H bond functionalization. *J. Am. Chem. Soc.* **144**, 2399–2414 (2022).
- Lepron, M. et al. Nanocatalyzed hydrogen isotope exchange. *Acc. Chem. Res.* **54**, 1465–1480 (2021).
- Atzrodt, J., Derdau, V., Kerr, W. J. & Reid, M. C@H functionalisation for hydrogen isotope exchange. *Angew. Chem. Int. Ed.* **57**, 3022–3047 (2018).
- Prakash et al. C–H deuteration of organic compounds and potential drug candidates. *Chem. Soc. Rev.* **51**, 3123 (2022).
- Di Martino, R. M. C., Maxwell, B. D. & Piralì, T. Deuterium in drug discovery: progress, opportunities and challenges. *Nat. Rev. Drug Discov.* **22**, 562–584 (2023).
- Mullard, A. First de novo deuterated drug poised for approval. *Nat. Rev. Drug Discov.* **21**, 623–625 (2022).
- Schmidt, C. First deuterated drug approved. *Nat. Biotechnol.* **35**, 493–494 (2017).
- Baratta, M. et al. 2023 White paper on recent issues in bioanalysis: deuterated drugs; LNP; tumor/FFPE biopsy; targeted proteomics; small molecule covalent inhibitors; chiral bioanalysis; remote regulatory assessments; sample reconciliation/chain of custody. *Bioanalysis* **16**, 307–364 (2024).
- Mullard, A. Deuterated drugs draw heavier backing. *Nat. Rev. Drug Discov.* **15**, 219–221 (2016).
- Qureshi, M. H. The Njarðarson group, The University of Arizona, top 200 small molecule drugs by sales in 2023 poster. <https://njarðarson.lab.arizona.edu/content/top-pharmaceuticals-poster> (2023).
- Kerr, W. J., Reid, M. & Tuttle, T. Iridium-catalyzed C–H activation and deuteration of primary sulfonamides: an experimental and computational study. *ACS Catal.* **5**, 402–410 (2015).
- Lauer, W. M. & Errede, L. A. The deuteration of aniline in the presence of raney alloy. *J. Am. Chem. Soc.* **20**, 5162–5163 (1954).
- Sajiki, H. et al. Aromatic ring favorable and efficient H–D exchange reaction catalyzed by Pt/C. *Tetrahedron Letters* **46**, 6995–6998 (2005).
- Derdau, V., Atzrodt, J., Zimmermann, J., Kroll, C. & Brückner, F. Hydrogen–deuterium exchange reactions of aromatic compounds and heterocycles by NaBD<sub>4</sub>-activated rhodium, platinum and palladium catalysts. *Chem. Eur. J.* **15**, 10397–10404 (2009).
- Valero, M. et al. NHC-stabilized iridium nanoparticles as catalysts in hydrogen isotope exchange reactions of anilines. *Angew. Chem. Int. Ed.* **59**, 3517–3522 (2020).
- Li, W. et al. Scalable and selective deuteration of (hetero) arenes. *Nat. Chem.* **14**, 334–341 (2022).
- Bourriquen, F., Rockstroh, N., Bartling, S., Junge, Kathrin & Beller, M. Manganese-catalysed deuterium labelling of anilines and electronrich (hetero)arenes. *Angew. Chem. Int. Ed.* **61**, e202202423 (2022).
- Elfinger, M. et al. General synthesis of alkyl amines via borrowing hydrogen and reductive amination. *Adv. Synth. Catal.* **365**, 4654–4661 (2023).
- Irrgang, T. & Kempe, R. Transition-metal-catalyzed reductive amination employing hydrogen. *Chem. Rev.* **120**, 9583–9674 (2020).
- Murugesan, K. et al. Catalytic reductive aminations using molecular hydrogen for synthesis of different kinds of amines. *Chem. Soc. Rev.* **49**, 6273 (2020).
- Dong, B. et al. Heterogeneous Ru-based catalysts for one-pot synthesis of primary amines from aldehydes and ammonia. *Catalysts* **5**, 2258–2270 (2015).
- Nishimura, S., Mizuhori, K. & Ebitani, K. Reductive amination of furfural toward furfurylamine with aqueous ammonia under hydrogen over Ru-supported catalyst. *Res. Chem. Intermed.* **42**, 19–30 (2016).
- Komanoya, T., Kinemura, Takashi, Kita, Y., Kamata, K. & Hara, M. Electronic effect of ruthenium nanoparticles on efficient reductive amination of carbonyl compounds. *J. Am. Chem. Soc.* **139**, 11493–11499 (2017).
- Guo, W., Tong, T., Liu, Guo, Y. & Wang, Y. Morphology-tuned activity of Ru/Nb<sub>2</sub>O<sub>5</sub> catalysts for ketone reductive amination. *ChemCatChem* **11**, 4130–4138 (2019).
- Liang, G. et al. Production of primary amines by reductive amination of biomass derived aldehydes/ketones. *Angew. Chem. Int. Ed.* **56**, 3050–3054 (2017).

28. Chatterjee, M., Ishizaka, T. & Kawanami, H. Reductive amination of furfural to furfurylamine using aqueous ammonia solution and molecular hydrogen: an environmentally friendly approach. *Green Chem.* **18**, 487 (2016).
29. Jiang, S. et al. Selective synthesis of THF-derived amines from biomass-derived carbonyl compounds. *ACS Catal.* **9**, 8893–88902 (2019).
30. Jagadeesh, V. et al. MOF-derived cobalt nanoparticles catalyze a general synthesis of amines. *Science* **358**, 326–332 (2017).
31. Hahn, G., Kunas, P., de Jonge, N. & Kempe, R. General synthesis of primary amines via reductive amination employing a reusable nickel catalyst. *Nat. Catal.* **2**, 71–77 (2019).
32. Zhang, Y., Yang, H., Chi, Q. & Zhang, Z. Nitrogen-doped carbon-supported nickel nanoparticles: a robust catalyst to bridge the hydrogenation of nitriles and the reductive amination of carbonyl compounds for the synthesis of primary amines. *ChemSusChem* **12**, 1246–1255 (2019).
33. Yuan, H. et al. Reductive amination of furanic aldehydes in aqueous solution over versatile Ni<sub>y</sub>AlO<sub>x</sub> catalysts. *ACS Omega* **4**, 2510–2516 (2019).
34. Bäumler, C., Bauer, C. & Kempe, R. The synthesis of primary amines through reductive amination employing an iron catalyst. *ChemSusChem* **13**, 3110–3114 (2020).
35. Long, X. et al. Graphitic phosphorus coordinated single Fe atoms for hydrogenative transformations. *Nat. Commun.* **11**, 4074 (2020).
36. Qi, H. et al. Highly selective and robust single-atom catalyst Ru<sub>1</sub>/NC for reductive amination of aldehydes/ketones. *Nat. Commun.* **12**, 3295 (2021).
37. Li, W., Yang, J., Wang, D. & Li, Y. Striding the threshold of an atom era of organic synthesis by single-atom catalysis. *Chem* **8**, 119–140 (2022).
38. Wang, A., Li, J. & Zhang, T. Heterogeneous single-atom catalysis. *Nat. Rev. Chem.* **2**, 65–81 (2018).
39. Singh, B. et al. Single-atom (iron-based) catalysts: synthesis and applications. *Chem. Rev.* **121**, 13620–13697 (2021).
40. Qi, H. et al. Water-promoted carbon-carbon bond cleavage employing a reusable Fe single-atom catalyst. *Angew. Chem. Int. Ed.* **62**, e202311913 (2023).
41. Ji, S. et al. Matching the kinetics of natural enzymes with a single-atom iron nanozyme. *Nat. Catal.* **4**, 407–417 (2021).
42. Liu, W. et al. Discriminating catalytically active FeN<sub>x</sub> species of atomically dispersed Fe–N–C catalyst for selective oxidation of the C–H bond. *J. Am. Chem. Soc.* **139**, 10790–10798 (2017).
43. Zhang, J., Yang, H. & Liu, B. Coordination engineering of single-atom catalysts for the oxygen reduction reaction: a review. *Adv. Energy Mater.* **11**, 2002473 (2021).
44. Bates, S. et al. Heterogeneous M–N–C catalysts for aerobic oxidation reactions: lessons from oxygen reduction electrocatalysts. *Chem. Rev.* **123**, 6233–6256 (2023).
45. Chen, Y. et al. Single-atom catalysts: synthetic strategies and electrochemical applications. *Joule* **2**, 1242–1264 (2018).
46. Ren, Y. et al. Unraveling the coordination structure-performance relationship in Pt<sub>1</sub>/Fe<sub>2</sub>O<sub>3</sub> single-atom catalyst. *Nat. Commun.* **10**, 4500 (2019).
47. Kopf, S., Neumann, H. & Beller, M. Manganese-catalyzed selective C–H activation and deuteration by means of a catalytic transient directing group strategy. *Chem. Commun.* **57**, 1137 (2021).
48. Jagadeesh, V. et al. Nanoscale Fe<sub>2</sub>O<sub>3</sub>-based catalysts for selective hydrogenation of nitroarenes to anilines. *Science* **342**, 1073–1076 (2013).
49. Yang, H. et al. A universal ligand mediated method for large scale synthesis of transition metal single atom catalysts. *Nat. Commun.* **10**, 4585 (2019).
50. Yang, J. et al. Dynamic behavior of single-atom catalysts in electrocatalysis: identification of Cu–N<sub>3</sub> as an active site for the oxygen reduction reaction. *J. Am. Chem. Soc.* **143**, 14530–14539 (2021).
51. Kruse, J. et al. Phosphorus L<sub>2,3</sub>-edge XANES: overview of reference compounds. *J. Synchrotron Rad.* **16**, 247–259 (2009).
52. Wang, Q. et al. Atomic metal–non-metal catalytic pair drives efficient hydrogen oxidation catalysis in fuel cells. *Nat. Catal.* **6**, 916–926 (2023).
53. Ding, J. et al. Room-temperature chemoselective hydrogenation of nitroarene over atomic metal–nonmetal catalytic pair. *Adv. Mater.* <https://doi.org/10.1002/adma.202306480> (2023).
54. Zhang, C. et al. Single-atomic ruthenium catalytic sites on nitrogen-doped graphene for oxygen reduction reaction in acidic medium. *ACS Nano* **11**, 6930–6941 (2017).
55. Allen, L. C. Electronegativity is the average one-electron energy of the valence-shell electrons in ground-state free atoms. *J. Am. Chem. Soc.* **111**, 9003–9014 (1989).
56. Qi, H. et al. Synthesis of piperidines and pyridine from furfural over a surface single-atom alloy Ru<sub>1</sub>Co<sub>NP</sub> catalyst. *Nat. Commun.* **14**, 6329 (2023).
57. Kresse, G. & Furthmüller, J. Efficiency of ab-initio total energy calculations for metals and semiconductors using a plane-wave basis set. *Comput. Mater. Sci.* **6**, 15–50 (1996).
58. Kresse, G. & Joubert, D. From ultrasoft pseudopotentials to the projector augmented-wave method. *Phys. Rev. B* **59**, 1758–1775 (1999).
59. Perdew, J. P. et al. Atoms, molecules, solids, and surfaces: applications of the generalized gradient approximation for exchange and correlation. *Phys. Rev. B* **46**, 6671–6687 (1992).
60. Monkhorst, H. J. & Pack, J. D. Special points for brillouin-zone integrations. *Phys. Rev. B* **13**, 5188–5192 (1976).
61. Jónsson, H., Mills, G. & W. Jacobsen, K. Classical and Quantum Dynamics in Condensed Phase Simulations 385–404 (World Scientific, Hackensack, 1998).
62. Henkelman, G. & Jonsson, H. A dimer method for finding saddle points on high dimensional potential surfaces using only first derivatives. *J. Chem. Phys.* **111**, 7010–7022 (1999).
63. Wang, V. et al. VASPKIT: a user-friendly interface facilitating high-throughput computing and analysis using VASP code. *Comput. Phys. Commun.* **267**, 108033 (2021).
64. Becke, A. D. Density-functional thermochemistry. III. The role of exchange. *J. Chem. Phys.* **98**, 5648–5652 (1993).
65. Schäfer, A., Huber, C. & Ahlrichs, R. Fully optimized contracted Gaussian basis sets of triple zeta valence quality for atoms Li to Kr. *J. Chem. Phys.* **100**, 5829–5835 (1994).
66. Frisch, M. J. et al. Gaussian 16, revision A.03 (Gaussian Inc., Wallingford, 2016).

## Acknowledgements

Y.R. thanks the National Key R&D Program of China (2023YFA1506603). H.Q. thanks the Alexander von Humboldt Foundation (CHN 1220532 HFST-P), Marie Skłodowska-Curie Actions Postdoctoral Fellowships (101107009-AtomCat4Fuel) and UKRI (EP/Y029305/1). We thank the Beamline BL14W of the Shanghai Synchrotron Radiation Facility (SSRF) and beamline MCD-A at the National Synchrotron Radiation Laboratory (NSRL) in Hefei, China for providing sufficient beamline time.

## Author contributions

H.Q. conceived the idea, performed the catalysts preparation, characterizations, catalytic performance test and wrote this manuscript. Y.J. and H.J. helped to perform DFT calculations. J.D., Y.R. and Y.Q. helped to do the HAADF-STEM, XAS characterizations, and revise the manuscript. N.D., B.Z., and S.T. helped to analyze characterization results and revise the manuscript. K.J., H.J., G.H., and M.B. directed the project and revised the manuscript. All the authors discussed the results and commented on the manuscript.

## Competing interests

The authors declare no competing interests.

## Additional information

**Supplementary information** The online version contains supplementary material available at <https://doi.org/10.1038/s41467-024-55722-9>.

**Correspondence** and requests for materials should be addressed to Yujing Ren, Kathrin Junge, Haijun Jiao, Graham J. Hutchings or Matthias Beller.

**Peer review information** *Nature Communications* thanks Rhett Kempe and the other, anonymous, reviewer(s) for their contribution to the peer review of this work. A peer review file is available.

**Reprints and permissions information** is available at <http://www.nature.com/reprints>

**Publisher's note** Springer Nature remains neutral with regard to jurisdictional claims in published maps and institutional affiliations.

**Open Access** This article is licensed under a Creative Commons Attribution-NonCommercial-NoDerivatives 4.0 International License, which permits any non-commercial use, sharing, distribution and reproduction in any medium or format, as long as you give appropriate credit to the original author(s) and the source, provide a link to the Creative Commons licence, and indicate if you modified the licensed material. You do not have permission under this licence to share adapted material derived from this article or parts of it. The images or other third party material in this article are included in the article's Creative Commons licence, unless indicated otherwise in a credit line to the material. If material is not included in the article's Creative Commons licence and your intended use is not permitted by statutory regulation or exceeds the permitted use, you will need to obtain permission directly from the copyright holder. To view a copy of this licence, visit <http://creativecommons.org/licenses/by-nc-nd/4.0/>.

© The Author(s) 2024